Eleventh International Conference on Computational Fluid Dynamics (ICCFD11), Maui, Hawaii, USA, July 11-15, 2022

ICCFD11-2022-2701

Receptivity of the BoLT-2 Boundary Layer to Freestream Disturbances

Zachary M. Johnston and Graham V. Candler
University of Minnesota
Minneapolis, MN, USA.

June 24, 2022

Abstract: Boundary layer disturbances in the Boundary Layer Turbulence (BoLT-2) flowfield are investigated using a low-dissipation numerical method at flight conditions. Unsteady simulations using US3D are performed with a freestream forcing function so that disturbances are passed through the bow shock and are meant to represent the effects of freestream turbulence. Modal decomposition analysis is applied to datasets obtained from high-fidelity computations in order to understand the relevant transition mechanisms potentially present in flight. This is motivated by the fact that the disturbance environment of quiet wind tunnels remains reasonably low up to a particular range of Reynolds number conditions before wind tunnel noise can significantly contribute to early transition. Therefore, this work reveals the dominant transition mechanisms contributing to the transition process on BoLT-2 when introducing freestream disturbances. Modal analysis is performed with Spectral Proper Orthogonal Decomposition (SPOD) to identify modes associated with significant disturbance amplification in regions of physical instability.

Keywords: Hypersonic Flow, Boundary Layer Transition, Computational Fluid Dynamics, BOLT-II.

1 Introduction

Understanding transition mechanisms in hypersonic boundary layers is important for predictive design and control of aerospace vehicles. This is due to the fact that laminar-turbulent transition of boundary layer flows have a direct impact on surface skin friction and aerodynamic heating affecting hypersonic vehicle performance. Transition studies for canonical flow problems (e.g. cones, flat plates, or wedges) have provided fundamental understanding, but at the expense of using analysis tools that are not guaranteed to scale well when applied to realistic flight geometries or flow conditions. To address some of the unsolved problems, the BoLT-2 hypersonic flight experiment is meant to collect flight data to help verify and develop the tools for boundary layer transition and turbulence studies to improve predictive capabilities. Recent simulations and analysis of the 25% subscale BoLT-2 geometry [1] have revealed breakdown to occur near crossflow vortices between the centerline and swept leading edge. Leading DMD mode shapes obtained from Streaming Total Dynamic Mode Decomposition (STDMD) showed that the strongest perturbations are present in the strong shear regions of stationary crossflow. Therefore, this suggests that breakdown within the subscale BoLT-2 configuration is initiated by the secondary instability of stationary crossflow vortices in the region showing evidence of Mack's second mode growth. It is still unclear how the developing rollup in the boundary layer is altered with respect to flight Reynolds numbers, Mach numbers, wall boundary conditions, and roughness [2, 3]. Additionally, the effect of the nosetip on the transition process on BoLT-2 has not been extensively studied.

Non-modal growth mechanisms along the centerline may contribute to early transition, and the high curvature of the bow shock could act as a source of vorticity that has an influence on instabilities downstream. These mechanisms may be dominant at high Reynolds numbers and total enthalpy conditions experienced in flight, but not at the conditions used in subscale wind tunnel tests. This is important since ground test campaigns are heavily used to dictate vehicle design but are restricted to flow regimes where the flow is expected to remain laminar or at most transitional. Higher Reynolds number conditions can be achieved in wind tunnels to observe turbulent heating but at the cost of unrealistic acoustic noise levels that are not representative of flight. Therefore, in this work, we seek to investigate the receptivity of the BoLT-2 boundary layer by performing forced DNS at a flight condition of the nominal trajectory that is at the same unit Reynolds number as a wind tunnel condition from the Mach 6 Quiet Wind Tunnel (M6QT) at Texas A&M University. To reduce computational expense and focus the investigation on receptivity effects, the majority of the simulations and analysis are conducted for the nosetip. Recent work has shown that a dominant flow response for blunted nosetips of straight cone configurations appears in the form of low-frequency steady streamwise structures, set off by freestream noise and surface roughness [4]. The amplification of this response scales with Reynolds number and nosetip bluntness. The non-modal growth mechanism likely exists near the leading edge of the BoLT-2 geometry, and could be a dominant response at the higher Reynolds numbers expected in flight. Therefore, both the flight and subscale configurations are simulated to investigate this mechanism and quantify the disturbance amplification spatially and temporally.

The scope of this paper is to identify relevant boundary layer modes corresponding to disturbance amplification of local flow quantities resulting from the receptivity of the BoLT-2 boundary layer to stochastic freestream forcing. The modes are associated with transition mechanisms that may contribute to early transition at high flight Reynolds numbers. High fidelity simulations of the Navier-Stokes equations are computed for the flight and subscale configurations. Stochastic freestream forcing is applied to five flow quantities such that the local disturbance energy for a given inflow cell remains low and disturbance fluctuations remain small relative to the freestream values. Lastly, the boundary layer flow state at an actual flight condition is performed to investigate the growth of disturbances leading to transition and to identify the boundary layer instabilities that are present. Since broadband forcing is applied to the flowfield, spectral proper orthogonal decomposition (SPOD) is chosen as the analysis tool to extract modes based on the covariance of the local disturbance fluctuations relative to the mean flow state. This allows us to identify statistically optimized oscillating modes associated with boundary layer instabilities.

The remainder of the paper is organized as follows: the flight geometry and flow conditions are introduced, next the computational methodology, followed by baseflow flow state comparison, then the modal analysis results are discussed, and finally conclusions and future work are summarized.

2 Geometry and Flow Conditions

The BoLT-2 geometry has been introduced in previous papers and is derived from the original BoLT geometry designed by the University of Minnesota in collaboration with AFRL [5]. The BoLT and BoLT-2 geometries are identical up to 0.866 m, at which the BoLT-2 team extended the geometry with a continuation of surface continuity up to 1.0 m for the flight geometry. The geometry is shown in Fig. 1 and contains a cylindrical leading edge that revolves to four swept leading edges and joined by concave surfaces in the azimuthal direction.

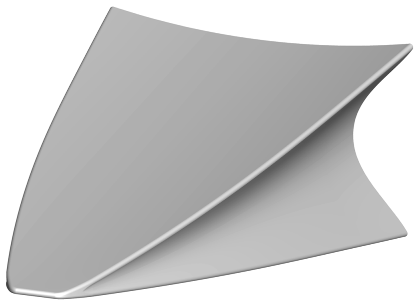

Figure 1: BoLT-2 flight geometry.

Definition	Value
Nose radius, r_f	5 mm
Characteristic length, L_f	1.0 m
Truncated length, $L_{f,t}$	0.1 m

Table 1: Flight Configuration

Definition	Value
Nose radius, r_s	1.25 mm
Characteristic length, L_s	0.25 m
Truncated length, $L_{s,t}$	0.025 m

Table 2: 25% Subscale Configuration

The unit Reynolds number condition was chosen since it is close to the maximum Reynolds number condition under quiet flow conditions in the Mach 6 Quiet Tunnel (M6QT) at Texas A&M University. The flight condition relative to the nominal BoLT-2 trajectory is shown in Fig. 2 along with the descent window where transition is expected to occur. To be clear, the flight conditions of Table 2 correspond to the projected nominal flight trajectory before the flight test was conducted and not from the actual flight trajectory. In the actual flight, the vehicle experienced Mach Numbers just over 6. Nonetheless, the flight condition was chosen to have the same unit Reynolds number to show the effects of scaling.

Condition	M_∞	U_∞ (m/s)	ρ_∞ (kg/m^3)	T_∞ (K)	T_{wall} (K)	Re/m (m^{-1})
Subscale (1)	5.9	870.3	0.0418	52.15	300	10.3×10^6
Flight (2)	5.6	1645.3	0.0895	216.96	300	10.3×10^6
Flight (3)	5.5	1658.4	0.0231	230.85	300	2.57×10^6

Table 3: Freestream Conditions

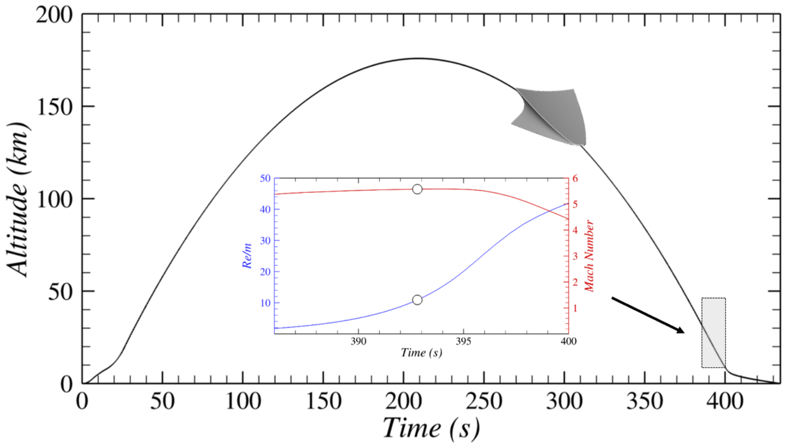

Figure 2: Nominal BoLT-2 flight trajectory.

3 Computational Methodology

To study the receptivity response, we perform simulations on the nosetip portion such that modal growth remains low. NPSE analysis [6] of a flow state at a similar nominal flight condition shows that disturbance amplification is low up to 30% of the geometry length. Therefore, the end of the computational domain was chosen to be at $x/L = 10\%$ of the research geometry length in the x-direction in order to study nosetip receptivity and save computational resources. The top half of the geometry is included in the region of interest to account for three-dimensional flow effects.

The boundary conditions are shown in Fig. 3 and include a freestream uniform supersonic inflow (hidden), isothermal wall with no-slip (grey), outflow (red), and a symmetry plane (blue) in the xz-plane. The isothermal wall is imposed in order to be consistent with the subscale configuration. The isothermal wall was chosen to reduce the parameter space since we are interested in isolating the effects of Reynolds number on the local boundary layer state. For the same reason, the flow is assumed to be at zero degrees angle of attack and slideslip. A quarter of the full domain is simulated later on to investigate the transition process downstream.

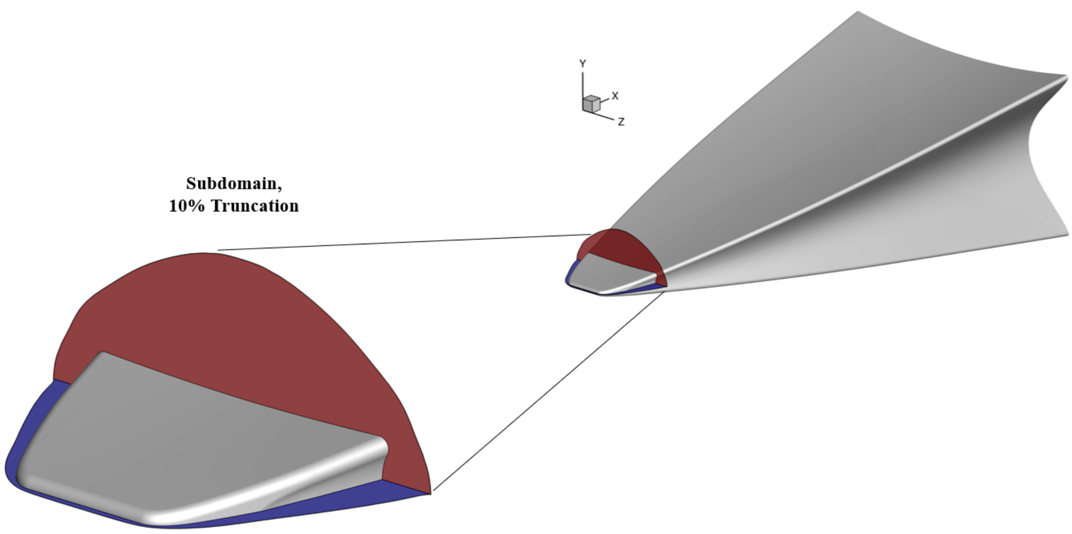

Figure 3: Truncated domain for high resolution nosetip simulations.

3.1 Governing Equations

The three-dimensional compressible Navier-Stokes equations are solved using the unstructured finite volume code, US3D, developed at the University of Minnesota [7]. The code and numerical method have been extensively tested and validated for a variety of unsteady compressible flow problems in the past. The simulations performed in this paper solve the compressible Navier-Stokes equations for a perfect gas in conservation form,

$$\frac{\partial \mathbf{U}}{\partial t} + \frac{\partial}{\partial x_i}\left(\mathbf{F}_j^c - \mathbf{F}_j^v\right) = 0 \tag{1}$$

The state vector is represented by $\mathbf{U} = [\rho, \rho u_i, E]^T$ and the components of the flux vector, $\mathbf{F}$, are represented by the convective flux, $\mathbf{F}_j^c = [\rho u_j, \rho u_i u_j + \delta_{ij} p, (E+p)u_j]^T$, and the diffusive flux, $\mathbf{F}_j^v = [0, \sigma_{ij}, u_i\sigma_{ij} - q_j]^T$. Sutherlands Law is used to account for the effect of temperature on viscosity using $\mu_o = 1.458\times10^{-6}$ kg/m·s and $T_o = 110.3$K. The heat flux is derived from Fourier's Law of heat conduction and related by the thermal gradient. The thermal conductivities for the translational and rotational energy modes are from an Eucken relation with a ratio of specific heat as $\gamma = 1.4$.

3.2 Numerical Method

The governing equations were solved in conservative form with a finite volume formulation and using a gradient scheme for the spatial discretization of the convective flux evaluation. All simulations evaluate the convective flux by reconstructing variables at each face for the symmetric flux using a sixth-order gradient based interpolation [8],

$$\phi_{i+1/2} = \frac{(\phi_i + \phi_{i+1})}{2} + \frac{8(\delta\phi_i + \delta\phi_{i+1})}{15} - \frac{(\delta\phi_{i-1} + \delta\phi_{i+2})}{45}, \tag{2}$$

where $\delta\phi_i$ corresponds to the dot product of the gradient of ϕ in cell i and the vector from the cell center of i to the face center of $i+1/2$. The viscous fluxes are computed using a second order central scheme. The low dissipation convective fluxes are split into a non-dissipative central component [9] and a dissipative component taking the following form,

$$\mathbf{F}_j^c = \mathbf{F}_{central} + \alpha\mathbf{F}_{diss}. \tag{3}$$

The dissipative flux, $\boldsymbol{F}_{diss}$, uses the dissipative portion of an upwind-biased TVD scheme based on flux vector splitting [10] with a MUSCL reconstruction for second-order accuracy [11]. The dissipative component of this scheme is made up of the dissipative flux based on a scalar dissipation factor, $\alpha \in [0,1]$, to minimize the percentage of the dissipative flux added. For the nosetip simulations, a lower bound of $\alpha = 0.01$ is set for numerical stability. Numerical dissipation is added by computing and storing the dilatation field from a second-order upwind solution and adding dissipation in regions of high compression with a user specified dilatation cutoff value which is then smoothed in space. This makes it so that the shock sensor is time independent following Knutson et al. [12].

In the case where the flow may experience breakdown, a custom shock sensor is used for simulations which extend the full length of the BoLT-2 geometry. This is because the flow state may evolve and should not be assumed to remain stable. In the case of significant disturbance amplification, a poor choice of shock sensor may activate a higher portion of numerical dissipation resulting in damped disturbance amplitudes. Therefore, the dissipation is tuned to the dilatation field using a compression based shock sensor. Where ϵ is a tuning parameter of 0.15, U_∞ is the freestream velocity, and δ is the maximum boundary layer thickness. A value for ϵ between 0.05 and 0.5 is typically sufficient for simulating most boundary layer stability problems. Additionally, a lower bound of $\alpha = 0.1$ was set for numerical stability. A higher grid resolution is required near the centerline roll-up if a lower dissipation scheme is used. The base shock sensor takes the following form:

$$\alpha = \frac{-\left(\nabla \cdot \mathbf{u}\right)}{\left[\left|\nabla \times \mathbf{u}\right| + \epsilon \cdot \frac{U_\infty}{\delta}\right]} \tag{4}$$

Implicit time integration is used in this work to obtain converged solutions within a reasonable amount of time. Implicit time integration is achieved by linearizing the fluxes in time and approximately solving the resulting linear system of equations using Data-Parallel Line Relaxation (DPLR) [13]. The steady-state solutions are obtained using first-order implicit time integration. For the unsteady simulations, a time accurate implicit method is necessary since amplification of boundary layer instabilities can be severely attenuated. In the present work, we use the second-order backward differentiation formula (BDF2) with Newton's method to solve the nonlinear equations [14]. The linear system is solved using line relaxation at each Newton subiteration where three subiterations are applied in this work.

4 Baseflow States

4.1 Nosetip Baseflow States

To first demonstrate the effects of higher Reynolds numbers relative to lower Reynolds numbers observed in previous work [15, 16], the baseflow state is computed using the conditions from Table 2. The hypersonic flow around the geometry produces a bow shock with varying three-dimensional curvature and the regions of sharpest bow shock curvature contain a significant presence of post-shock vorticity. The inviscid flow state described by Thome et al. [16] showed that the distribution of vorticity on the top surface contains two distinct regions with highly localized vorticity magnitude near the centerline and close to the swept leading edge. Fig. 4 shows how the vorticity magnitude is distributed post-shock where the streamwise vorticity component (not shown) is largest closer to the centerline and partially contributes to the centerline roll-up downstream. Another vorticity contribution to the centerline roll-up originates where the two-dimensional cylindrical nosetip revolves to a swept leading edge. Furthermore, the left plot of Fig. 4 shows streamlines near the wall, originating from the post-shock region with the highest shock curvature. The local pressure gradients alter the path and the streamwise vorticity is negative downstream as denoted in the plot on the bottom, right. Local boundary layer edge streamlines have positive streamwise vorticity near the swept leading edge but are not shown. The plots on the right of Fig. 4 illustrate this and reveal an inflection point, characteristic of crossflow, at the positive and negative interface of the streamwise vorticity distributions. The streamwise vorticity distribution for the flight configuration is more compressed near the wall due to the thinner boundary layer relative to the subscale configuration. This is important to keep in mind since the vorticity distribution has a significant influence on the boundary layer state.

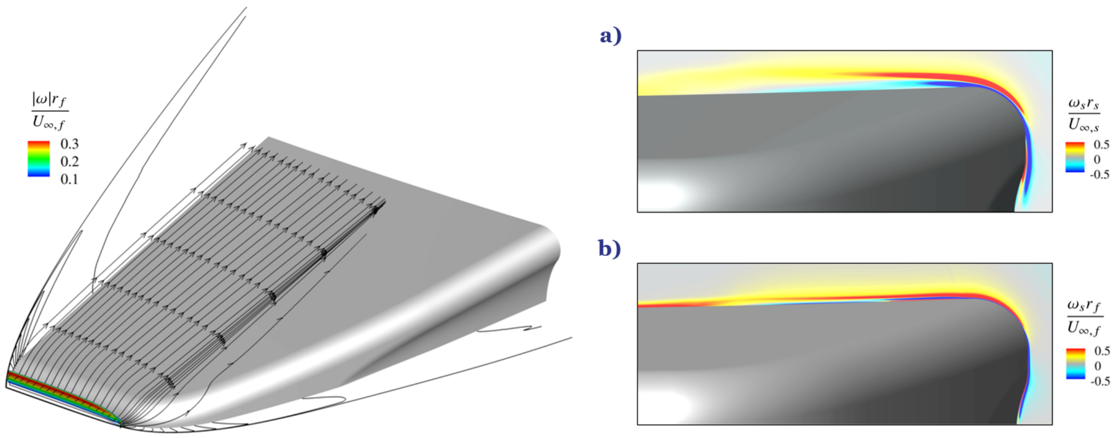

Figure 4: Left shows streamlines originating from regions with high vorticity magnitude for the flight configuration. Normalized streamwise vorticity is show on the right for a) the subscale configuration at condition 1 and b) flight configuration at condition 2.

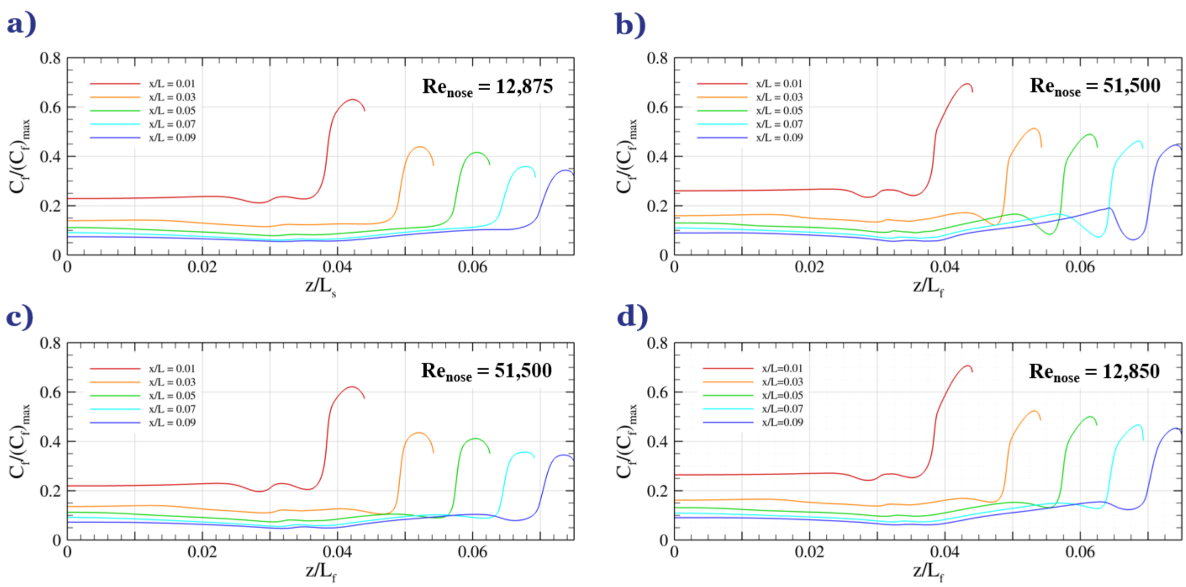

Figure 5: Normalized skin friction coefficients: a) subscale configuration at condition 1, b) flight configuration at condition 2, c) flight configuration at condition 1, and d) flight configuration at condition 3.

In order to quantify viscous effects, a normalized skin friction coefficient is calculated for comparison since we are comparing scaled geometries and flow conditions. The purpose of this is to elucidate the difference in viscous effects of the subscale configuration at wind tunnel conditions and the full scale configuration at flight conditions. The combination of flow conditions and geometry scaling have a significant influence on crossflow and this directly affects the skin friction. Therefore, the magnitude of the wall shear stress is calculated and non-dimensionalized by the corresponding freestream values. Next, the skin friction coefficient is normalized by the maximum skin friction coefficient on the wall and is located where the two-dimensional cylindrical nosetip revolves to a swept leading edge for all cases. Using a normalized skin friction coefficient allows us to make a direct comparison of the surface profiles. Fig. 5 shows the normalized skin friction coefficients where 5a) and 5c) are the same flow condition for the 25% subscale geometry and full-scale geometry, respectively. By scaling down the geometry, the trends of the normalized skin friction profiles of 5a) demonstrates that the flow state is representative of a slightly lower Reynolds number compared to 5c) which has a different nosetip Reynolds numbers.

Plots 5b), 5c), and 5d) are the full-scale geometry but at different freestream conditions. Making a comparison of the normalized skin friction profiles of 5c) and 5d) shows agreement and suggests that the boundary layer state using a wind tunnel condition (condition 1) scales approximately with the Reynolds number of a flight condition (condition 3) by a factor of 4. This is for the same geometry and isothermal wall temperature, despite having different freestream unit Reynolds numbers and total enthalpies. A comparison of 5b) and 5c) exemplifies that the trends of the surface profiles are independent of nosetip Reynolds number. The same trends in the normalized skin friction are also observed in the normalized heat transfer coefficient. Fig. 6 reveals how the heat transfer coefficient on the surface compares between the targeted cases, 6a) and 6b). Therefore, the normalized skin friction and heat transfer coefficient profiles reveal how wall quantities change with respect to viscous effects induced by the near wall crossflow inflection point. Note that the nosetip solution in 5a) and 6a) is representative of the wind tunnel condition used in past work [1].

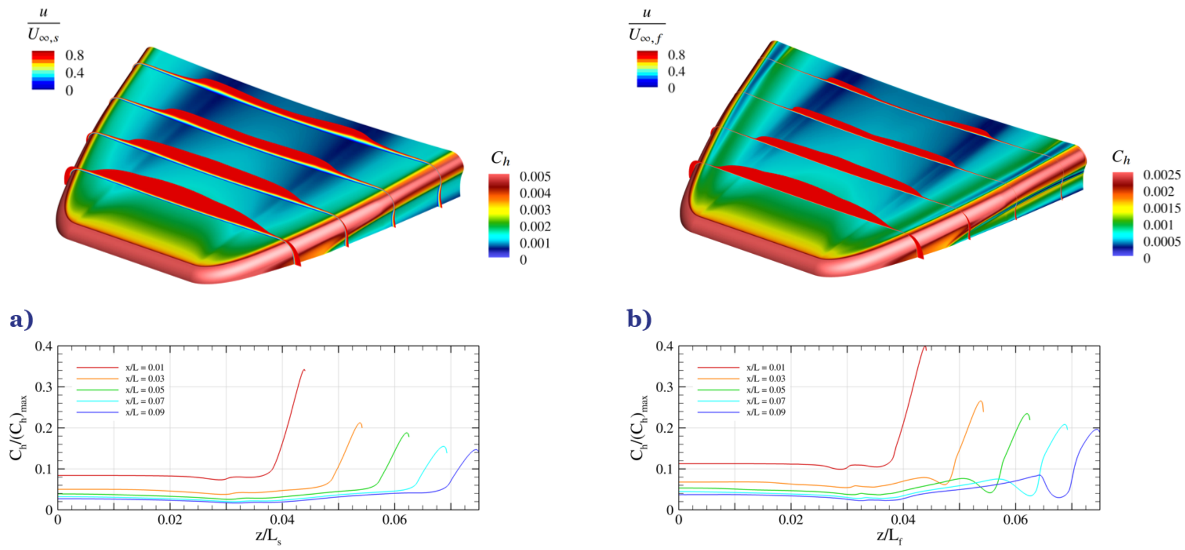

Figure 6: Steady-state flowfields of a) subscale configuration at condition 1 and b) flight configuration at condition 2. Streamwise velocity is normalized by the freestream value and the wall contours are the local heat flux normalized by the corresponding freestream conditions. Spanwise slices of the normalized heat transfer coefficients are below.

4.2 Flight Configuration Baseflow State

The viscous effects from the last section are governed by varying pressure gradients and contribute to the developing vortex structures downstream which are able to support various types of instabilities [17]. At subscale wind tunnel conditions, the boundary layer rolls-up between the centerline and swept leading edge and for a longer geometry stationary crossflow vortices develop - not to be confused with stationary crossflow instabilities. For the full scale geometry at a flight condition, Fig. 7 illustrates how the developing roll-up between the centerline and swept leading edge is different from a subscale setup with close to the same Mach number and unit Reynolds number from [15]. The most apparent difference is observed near the large-scale counter rotating vortex structures close to the centerline where secondary roll-up produces a vary thin boundary thickness. In the present literature, it is unclear how the secondary roll-up near the centerline drives transition and analysis later investigates this.

M_∞	U_∞ (m/s)	ρ_∞ (kg/m^3)	T_∞ (K)	T_{wall} (K)	Re/m (m^{-1})
6.09	1773.22	0.067	211.0	330	8.6×10^6

Table 4: BoLT-2 flight condition from actual flight trajectory. The isothermal wall temperature of this table is approximately the average temperature across thermocouple measurements at the end of the geometry. (Private Communication: Dr. Rodney Bowersox, TAMU)

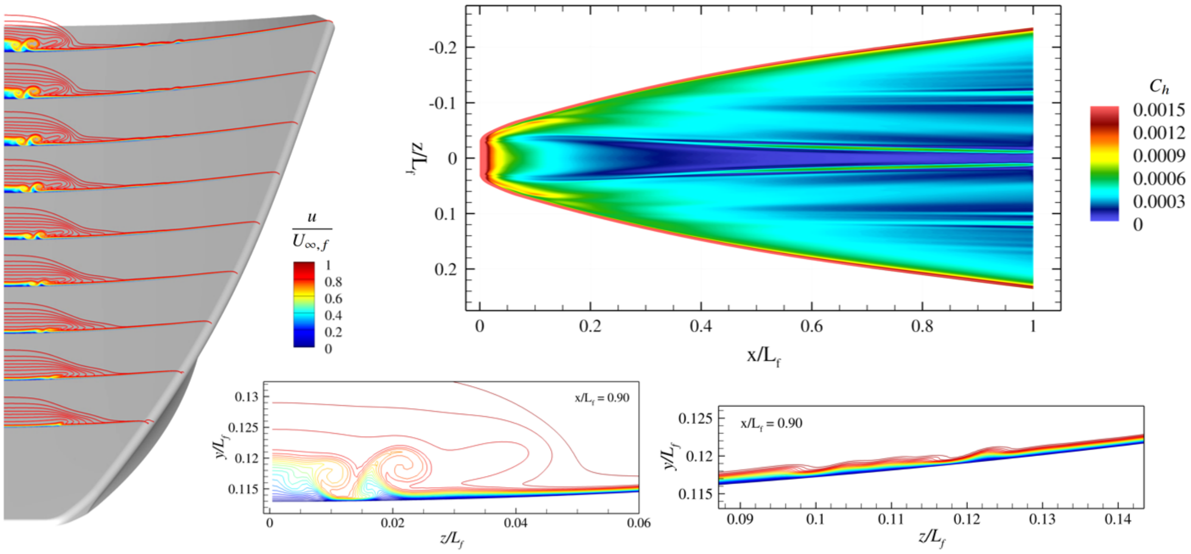

Figure 7: Streamwise velocity (left) and heat flux coefficient (right) of the flight configuration for an actual flight condition where the boundary layer is in a transitional state. The steady-state solution shown was obtained with first-order DPLR time integration [13].

5 Three-dimensional Perturbation Growth and Analysis

5.1 Unsteady Forcing: Freestream Disturbances

Before introducing disturbances, a steady-steady solution is converged and is defined as the baseflow state in this work. After the baseflow state is obtained, small amplitude disturbances in the primitive variables are introduced using a sustained, broadband stochastic forcing approach. The purpose of this is to force with white-noise so that the distinct shock structures filters the noise taking the form of three-dimensional post-shock waves. This is visualized in Fig. 8 showing temperature mode shapes in the entropy layer which contain very small amplitudes relative to perturbations in the boundary layer. The figure shows an example of how temperature is affected by three-dimensional waves produced by propagating the disturbances through the shock. This can be thought of as the superposition of acoustic, vortical, and entropic modes on temperature at discrete frequencies. The majority of the disturbance energy is contained in the low-frequency range from 5 kHz to 60 kHz, even though high-frequency modes of relatively small amplitude are present as well. Similar global modes have been studied using Input-Output (IO) analysis on cone geometries which take the form of low- and high- frequency mechanisms [18].

The fluctuations in the primitive variables are a function of a non-dimensional random number, $r_i \epsilon(-1, 1)$, obtained with a pseudo-random number generator that is computed at each time step. The amplitude, A, is non-dimensionalized and scaled using the Chu [19] energy norm so that the disturbance energy is very low relative to the total freestream energy. E_d is the non-dimensionalized disturbance energy, and is set such that the local disturbance energy cannot exceed 0.15% of the total freestream energy. The fluctuations in the five perturbations variables are set such that each value does not exceed 0.3% of the corresponding freestream value. This results in an amplitude, A, of 0.5 being specified. The disturbance forcing approach follows Melander et al. [4] and is shown below,

$$(u_r, v_r, w_r, T_r, \rho_r) = r_i \epsilon(-1, 1)$$
$$E_d = \left[{u_r}^2 + {v_r}^2 + {w_r}^2 + {T_r}^2 \frac{1}{\gamma(\gamma - 1){M_\infty}^2} + {\rho_r}^2 \frac{1}{\gamma {M_\infty}^2} \right]^{1/2} \tag{5}$$

$$(u', v', w', T', \rho') = A(u_r, v_r, w_r, t_r, \rho_r) \frac{1}{E_d} \mathrm{diag}(|\tilde{\mathrm{U}}|, |\tilde{\mathrm{U}}|, |\tilde{\mathrm{U}}|, \bar{\mathrm{T}}, \bar{\rho}) \tag{6}$$

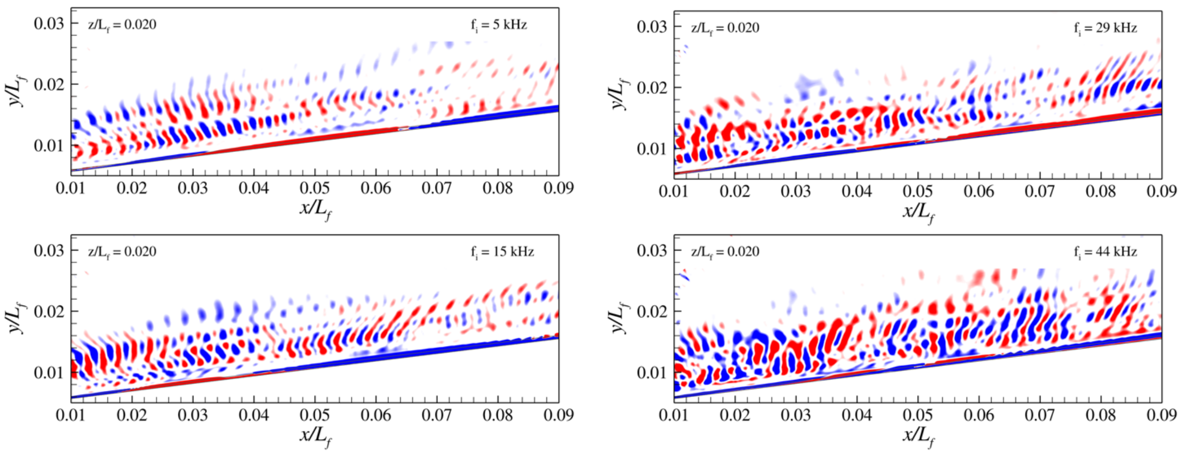

Figure 8: Temperature SPOD mode shapes of low-frequency modes in the entropy layer.

5.2 Spectral Proper Orthogonal Decomposition Analysis

In the current work we will utilize the spectral proper orthogonal decomposition (SPOD). This approach approximates the two-point space-time correlation (covariance) tensor associated with the flow response [20],

$$\mathbf{C}(x, x', t,' t) = \mathbb{E}\left(q(x, t)q(x', t)\right) \tag{7}$$

$q(x, t)$ is the state of interest and $\mathbb{E}$ is the expectation operator and can be thought of as an ensemble average of flow realizations or snapshots. For stationary states, an efficient implementation can be derived in the frequency domain by expanding the Fourier modes [21, 22],

$$\hat{q}(x, f) = \sum_{j=1}^{\infty} a_j(f)\psi_j(x, f) \tag{8}$$

where f is the temporal frequency and expansion coefficients are $a_j(f) = \langle \hat{q}(x, f), \psi_j(x, f)\rangle$ with an appropriate definition of the inner product $\langle \cdot, \cdot \rangle$ in the spatial domain. The SPOD algorithm used in this work is introduced in Towne et al. [21]. The choice of inner product defined by the weight matrix, W, is the compressible energy norm following the original derivation [19, 22]. The local cell volume is used to account for the spatially discretized integration while the perturbations quantities are the flow quantities with respect to the time-averaged value. Typically, the baseflow value is commonly used for boundary layer stability analysis and quantifying disturbance amplification. However, the time-averaged value was chosen to be the mean flow value in this work since modal analysis is performed on forced DNS datasets.

$$q = \begin{bmatrix} u' \\ v' \\ w' \\ \rho' \\ T' \end{bmatrix}, \qquad W = \int_V \begin{bmatrix} \overline{\rho} & & & & \\ & \overline{\rho} & & & \\ & & \overline{\rho} & & \\ & & & \frac{\overline{T}}{\gamma \overline{\rho} \overline{M}^2} & \\ & & & & \frac{\overline{\rho}}{\gamma(\gamma-1)\overline{T}\overline{M}^2} \end{bmatrix} dV \tag{9}$$

Stationary snapshots are taken of the unsteady simulations with the perturbations values obtained by subtracting off the time-averaged value. Since the flow is forced stochastically and is at a statistical steady-state, each snapshot is considered a separate run, and the resulting SPOD modes are the resolvent modes. Mode shapes and the energy gain associated of the corresponding mode are used to order each mode based on the contribution to the modal energy relative to the total modal energy. Since we are performing SPOD on five flow variables consistent with the compressible energy norm weighting, the modal energy is associated with the spatio-temporal disturbance energy contribution. Because the datasets are non-periodic in nature, a Hamming window using a specified window length with 50% overlap was used. The open-source, freely available software implementation of the SPOD algorithm was used for all results in this work (https://www.mathworks.com/matlabcentral/fileexchange/65683-spectralproper-orthogonal-decomposition-spod).

5.3 Data Collection and Sampling

Because of the size of the grids, the required data storage is prohibitively expensive if the entire solution were stored as a single snapshot for time-series data. Therefore, data was collected by storing cell centered data from cells that intersect specified x- and z-locations and are equally spaced in time. For visualization, the cell centered values were interpolated onto two-dimensional planes in space. The introduced modal analysis approach can be used to extract three-dimensional modes shapes. However, data storage is computationally expensive due to the size of the grids and required sampling.

Definition	
Simulation time step	10 ns
Number of Snapshots	2000
Snapshot Spacing	0.2 μs
Sampling Frequency	5.0 MHz
Snapshot Sequence	400 μs
Single Period Wave	2.5 kHz

Table 5: High-frequency Sampling

Definition	
Simulation time step	50 ns
Number of Snapshots	1000
Snapshot Spacing	2.0 μs
Sampling Frequency	500 kHz
Snapshot Sequence	2000 μs
Single Period Wave	0.5 kHz

Table 6: Low-frequency Sampling

In order to extract pertinent modal information using SPOD, the sampling has to be sufficiently high frequency and long duration to resolve and capture spatio-temporal information. The sampling parameters for low and high sampling rates are summarized in Tables 5 and 6, respectively. Note that the sampling parameters are slightly different since different simulation time steps were used and computational resources had to be accounted for. To post-process the solutions and save time series data for the entire domain, the storage space and potentially the analysis approach would have to change considerably if analysis were performed on the entire domain at once. This undertaking is outside the scope of this work, and therefore data collection and analysis is only conducted on individual slice datasets treated independently for the nosetip simulations. For the downstream SPOD analysis, multiple slice datasets were considered to show how the modes are correlated in space and time.

5.4 Grid Resolution Estimate and Sampling Convergence

All meshes in this work have grid alignment with the bow shock curvature. This is very important when passing disturbances through shocks since large variations in grid spacing and poor shock alignment can produce a significant amount of dispersive error. Therefore, we apply grid tailoring to ensure the grid is approximately orthogonal at the bow shock. We first compute the maximum of the pressure gradient in the wall-normal direction to locate the bow shock on an initial mesh, redistribute the grid points extending from the wall to the inflow, smooth along grid connected lines, and converge the solution on the tailored grid. If this is not accounted for, the numerical error in some cases can initiate transition aphysically when using high order, low dissipation numerical schemes. Furthermore, it is important that the grid has sufficient resolution to resolve relevant frequency content and to respect the wave damping characteristics of the numerical method used in the external forcing simulations. The grids in this work were create to resolve expected frequencies that correspond to boundary layer instabilities with the highest amplification from NPSE at close to the same condition [6]. The necessary grid resolution to properly capture turbulent length scales is estimated to be an order of magnitude greater.

The current grid that encompasses a quarter domain of the full geometry extent contains 600 million elements. The target grid spacing located at $x/L = 1.0$ near the centerline is slightly under-resolved, where the spanwise grid spacing is approximately one-third of the streamwise grid spacing at the end of the domain. This total grid size restriction is limited by the current data structure capabilities. The nosetip grids for both the 25% subscale and flight configurations have the same cell spacing distributions in every direction except the wall normal direction. To be clear, the same topology is used for the subscale configuration but the domain is scaled down to 25% of the full-scale size. The spacing of the first cell off the wall is adjusted for each configuration such that the $y+$ remains below 0.1 in the regions of interest. Recent grid estimates show that a $y+ < 0.1$ is sufficient to resolve the viscous stresses near the wall for most DNS calculations [23]. To demonstrate that the grids and sampling are converged for unsteady forcing simulations and spectral analysis, the full length grid is truncated to 28% of the domain length. This is chosen since the baseline grid has half the number of points distributed at the leading edge, half the spanwise grid resolution, and assumes a symmetry plane along the centerline.

Freestream forcing is applied to the truncated domain and the grid dimensions for the flight configuration are in Table 7. Time-series data is then collected at $z/L_f = 0.0755$ using the simulations and sampling parameters from Table 5 to capture a broader range of frequencies. This is due to the fact that past stability analysis for this geometry estimates modal growth for second-mode frequencies just over 800 kHz along the streamwise location selected. By performing SPOD on the collected time-series, a significant peak in the modal energies at a frequency of 820 kHz is present. The density perturbation mode shape shown in Figure 9

	Baseline (Quarter Domain)	Fine (Half Domain)
Streamwise Extent (L)	0.28 m	0.1 m
Total cell count	$141x10^6$	$139x10^6$
Leading edge points	40	110
Streamwise (ξ) points	1440	620
$\Delta\xi_{(}x/L = 0.1)$	0.19 mm	0.19 mm
Spanwise (ζ) points	410	1030
$\Delta\zeta(x/L = 0.1)$	0.28 mm	0.18 mm
Wall-normal (η) points	250	250
y^+_{max}	0.4	0.4
$y^+(x/L = 0.1)$	0.05	0.05

Table 7: Grid Metrics: Nosetip configurations

corresponds to a second-mode disturbance where the leading SPOD mode contributes to 90% of the local disturbance energy at the discrete frequency and spatial location. Additionally, SPOD modes shown in later sections are consistent with the modes extracted in the spanwise direction for both grids. This suggests that the baseline grid is sufficient for capturing desired spectral content. To ensure grid convergence, the fine grids were used for modal analysis at the leading edge nosetip. The sampling duration for the nosetip datasets was checked for convergence by sampling for longer duration. It was determined that the same modal energy peaks remained the same, and the values were relatively much higher than the peak of the sampling duration cutoff frequency.

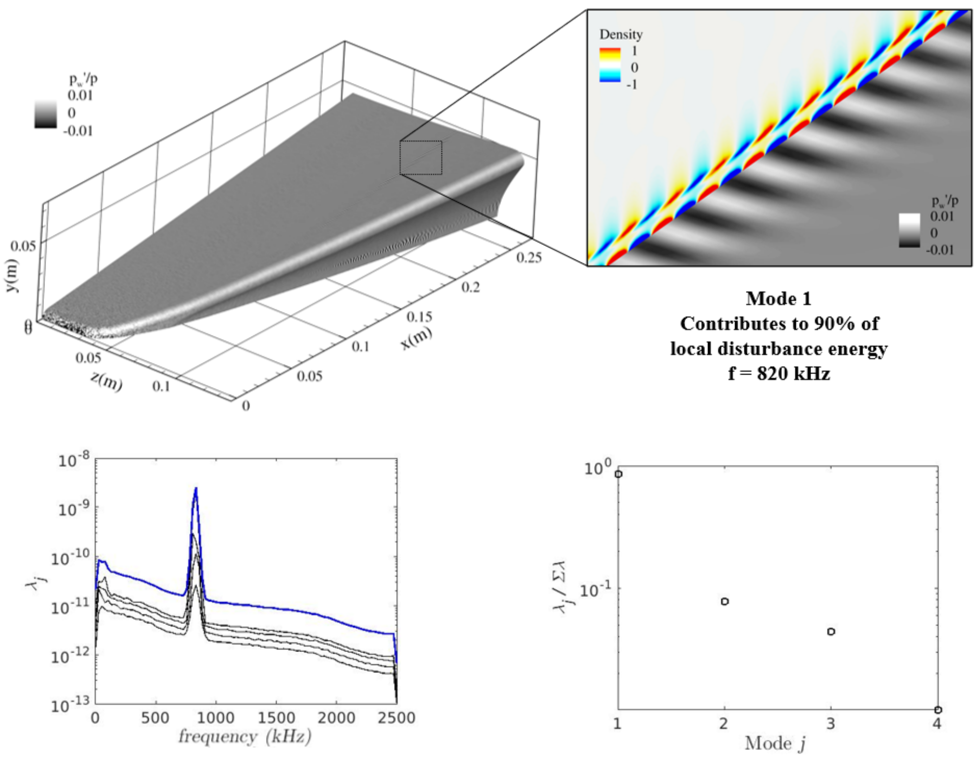

Figure 9: Leading SPOD mode shape for data collected at $z/L_f = 0.0755$ of the baseline mesh corresponds to second-mode disturbance and is consistent with NPSE estimates in terms of frequency, wavelength, and relative disturbance amplification.

6 Modal Analysis Results

6.1 Non-modal Growth Mechanisms

By forcing the flow-state using the numerical approach, streamwise structures develop near the nosetip of the geometry along with excitation of boundary layer instabilities later downstream. As mentioned by Bitter [24], it is common for non-modal growth to exhibit the "lift-up" effect [25] and takes the form of streamwise vortices and is similar to the structures near the leading edge. The source that is most likely to excite transient growth mechanisms has been thought to be roughness since surface roughness acts as a steady forcing source. This is due to the fact that the optimal growth for reattachment streaks within a hypersonic boundary layer occurs for zero frequency temporal wavenumbers with a spanwise wavenumber [26]. Vortical structures within a hypersonic boundary layer of a compression ramp extracted with Input-Output take the form of streamwise streaks and the streamwise velocity perturbations are associated with large, localized peaks in surface heating. A similar response was found for the nosetip of a cone configuration by Melander et al. [4]. This is a possible explanation for the developing streamwise structures contained within the centerline roll-up on the BoLT-2 geometry when utilizing a sustained, stochastic freestream forcing function as an input to the DNS.

Using the methodology introduced, snapshots were taken at the same non-dimensional locations of the 25% scaled configuration as the full scale configuration. SPOD modes shapes of streamwise velocity perturbations are plotted in Fig. 10 taken at $x/L_s = 0.025$ and 0.050. The spectrum containing the majority of the disturbance energy gain is around 5 kHz. Therefore, at both streamwise locations, Fig. 10 shows a strong signature in the power spectral density (blue-line) and modal energy spectrum of each SPOD mode (black) at 5 kHz where the SPOD mode shapes are also plotted. With SPOD, the data matrix is split into blocks and the windowed Fourier Transform is calculated and stored. This means there are a set of resolvent modes containing a portion of the modal energy at each discrete frequency depending on the window-length and sampling parameters. At $x/L_s = 0.050$, the leading SPOD mode with a frequency of 5 kHz contributes to 52% of the modal energy with a mean spanwise wavelength, λ_ζ, of 0.84 mm. The same modal contribution is contained in the streamwise direction at $z/L_s = 0.020$ with a mean streamwise wavelength, λ_ξ, of 5.3 mm. This is shown in Fig. 11 along with high frequency modes having frequencies of 65 kHz and 150 kHz. The 150 kHz mode has a relatively high PSD signature with the first SPOD mode having a 53% modal energy contribution. The low frequency mechanisms are slowly varying in space and time and are similar in shape to stationary crossflow structures induced by roughness [3]. Whereas the high frequency mode identified in the streamwise direction are consistent with expected wavelengths for high frequency travelling crossflow instability obtained with NPSE [6] near the swept leading edge.

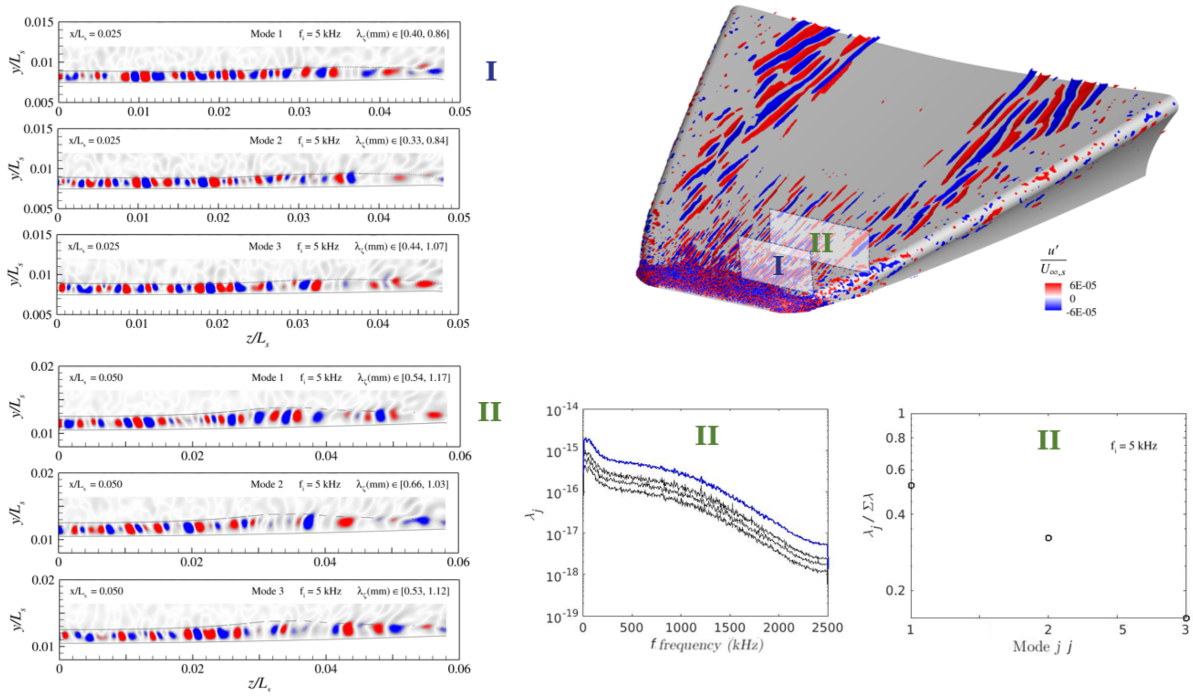

Figure 10: Leading SPOD Modes for dominant frequency of the subscale configuration at $x/L_s = 0.025$ and $x/L_s = 0.050$ and the spanwise wavelength defined as λ_ζ.

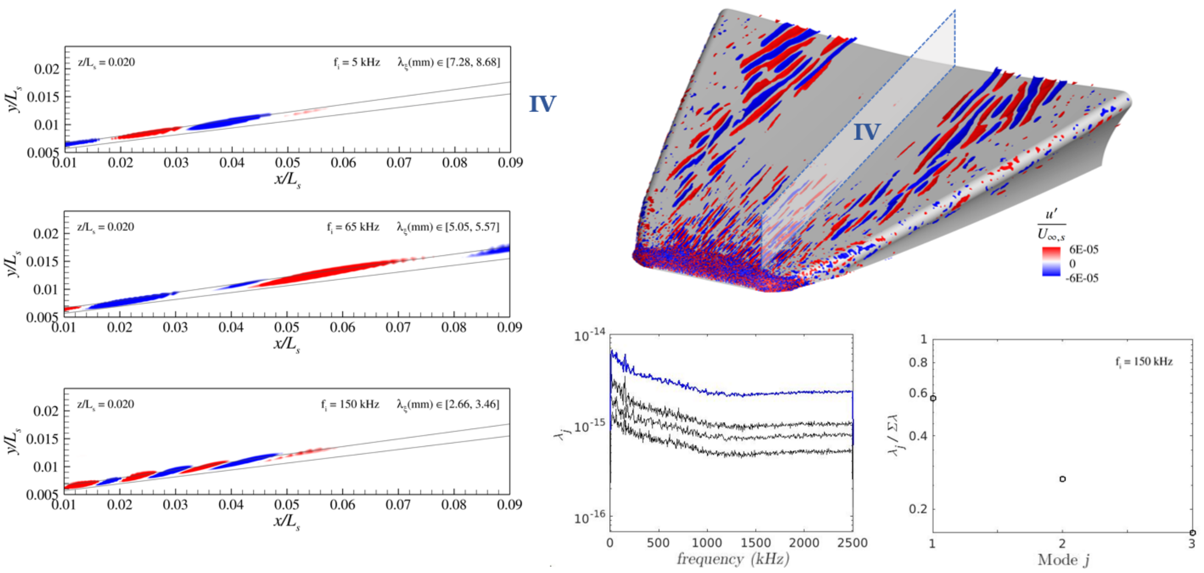

Figure 11: Leading SPOD Modes of the subscale configuration at $z/L_s = 0.02$ and the streamwise wavelength defined as λ_ξ.

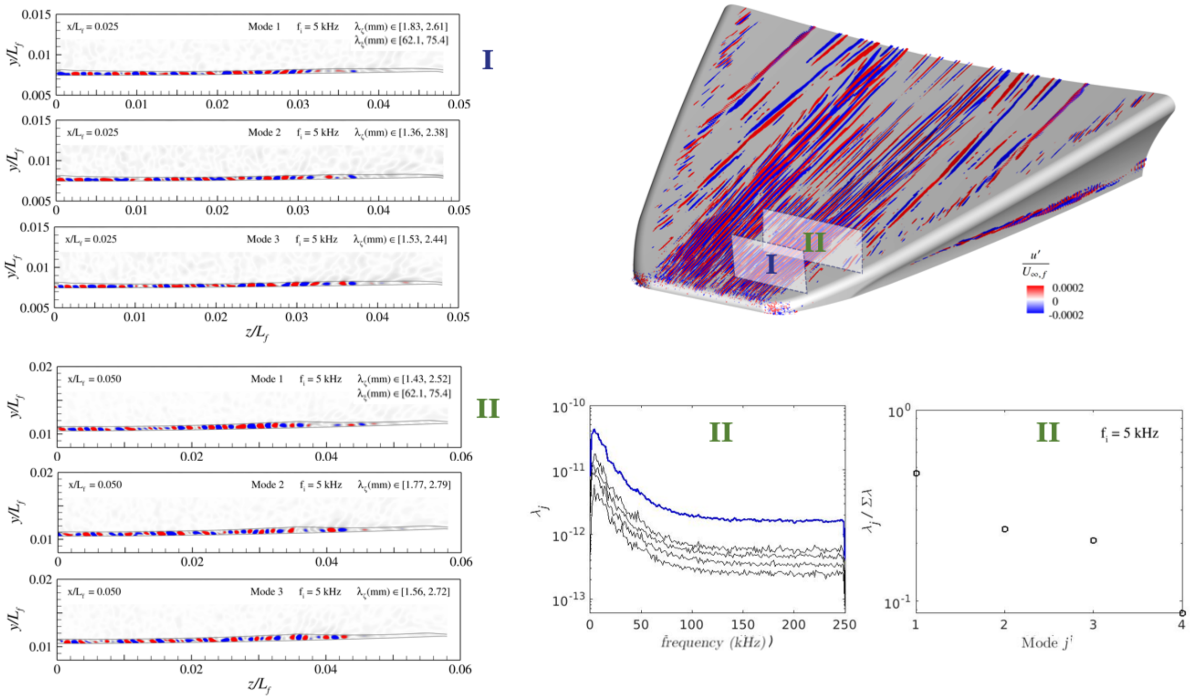

Figure 12: Leading SPOD Modes of the flight configuration at $x/L_f = 0.025$ and $x/L_f = 0.050$

The flight configuration has a similar modal energy spectrum as the subscale configuration since the majority of the modal energy is contained within the 4 kHz to 6 kHz frequency range. However, due to the thin boundary layer state the structures are contained within a shorter distance off the wall. The mean spanwise wavelength of the low-frequency structures range from 2.0 mm to 3.1 mm from $x/L_f = 0.025$ and 0.050, respectively. Whereas, the local spanwise wavelength scales with the local boundary layer thickness near the centerline by $\lambda_\zeta/\delta \sim 4$ for the flight configuration compared to $\lambda_\zeta/\delta \sim 2$ for the subscale configuration.

The amplification of disturbances by the low-frequency structures of the flight configuration is much greater than that of the subscale configuration. This suggests that the streamwise structures could potentially contribute to early transition at higher Reynolds numbers and can be influenced by the freestream environment or other external perturbation sources (i.e. roughness). In order to generate surface roughness, we utilize a probability density function to investigate the effects of roughness. Each wall node is perturbed using a random number, between (-1,1), and multiplied by a maximum amplitude. The displacement is smoothed along grid connected lines, similar to the approach used by Dinzl & Candler [27]. Previous work by Thome et al. [2] showed that different heating patterns are observed on the BoLT configuration using different roughness wavenumber distributions. However, a non-biased wavenumber distribution allows for an exploratory look at the flowfield response without filtering out potentially relevant disturbances. In this work, it was found that similar structures containing zero frequency temporal wavenumbers were excited using a maximum node displacement of 2 μm with a Gaussian distribution probability density function. This suggests steady forcing of the flow state seeds non-modal growth instabilities near the nosetip. At the current condition, the perturbation values are small suggesting it is unlikely to trip early transition at the flow conditions used in this paper.

6.2 Modal Growth Mechanisms

Due to the receptivity process, modal growth of instabilities becomes present further downstream. When considering the subscale configuration, the local disturbance amplitudes induced by the low-frequency structures start to decay near the centerline when travelling downstream. While crossflow instabilities begin to show strong signatures in the frequency spectrum ranging from 20 kHz to 40 kHz. Additionally, there is a presence of signatures lower than 20 kHz within the centerline roll-up ($x/L_s \,\epsilon\, [0, 0.04]$). However, the local disturbance energy is much higher closer to the swept leading edge between $x/L_s \,\epsilon\, [0.04, 0.1]$. It is in this region where SPOD mode shapes representative of travelling crossflow instabilities are prominent for the subscale configuration.

Contrary to the subscale configuration, the flight configuration shows strong signatures in the modal energy spectrum of the low-frequency modes and are contained within the centerline roll-up at approximately 20 kHz. Also, the spectrum shows strong signatures at 820 kHz, 1000 kHz, and 1660 kHz, and the resolvent modes of the respective frequencies are primarily located closer the the swept leading edge. The streamwise SPOD mode shape for the 820 kHz mode was shown previously in Section 5.4 and represents a Mack's second mode disturbance. The modal energy contribution is 99.8% for the first SPOD mode based on the spanwise collected dataset. Furthermore, the PSD peak is the highest at 820 kHz suggesting second-mode amplification is more profound for the flight configuration. The SPOD mode at 1000 kHz appears to represent second-mode disturbance amplification with a spanwise wavelength. Whereas, the 1660 kHz mode appears to be a secondary harmonic of the primary 820 kHz disturbance. At $x/L_f = 0.25$,$z/L_f = 0.0755$, the 820 kHz second-mode disturbance has a wavelength of $\lambda_\xi = 1.56$ mm which is approximately twice the boundary layer thickness resulting in a phase speed of $c_{ph} = 1275$ m/s. The frequency scales with the local boundary layer properties as $f \sim 0.4\frac{u_e}{\delta}$ for the flight configuration.

The local scaling for second-mode frequencies based on Stetson [28] predicts that second-mode frequencies scale with the boundary layer edge velocity and the local boundary layer thickness as $f \approx 0.4\frac{u_e}{\delta}$. Using the local edge velocity, 1502.8 m/s, and boundary layer thickness, 0.739 mm, estimates that the local frequency for second-mode would be approximately 814 kHz. This suggests that second-mode disturbance frequencies scale with the local flow properties on BoLT similar to the second-mode frequency estimate for hypersonic boundary layers introduced by Stetson. Additionally, this is consistent with the scaling of second-mode disturbance frequencies of the subscale BoLT configuration slightly further downstream as introduced by Knutson et al. [17].

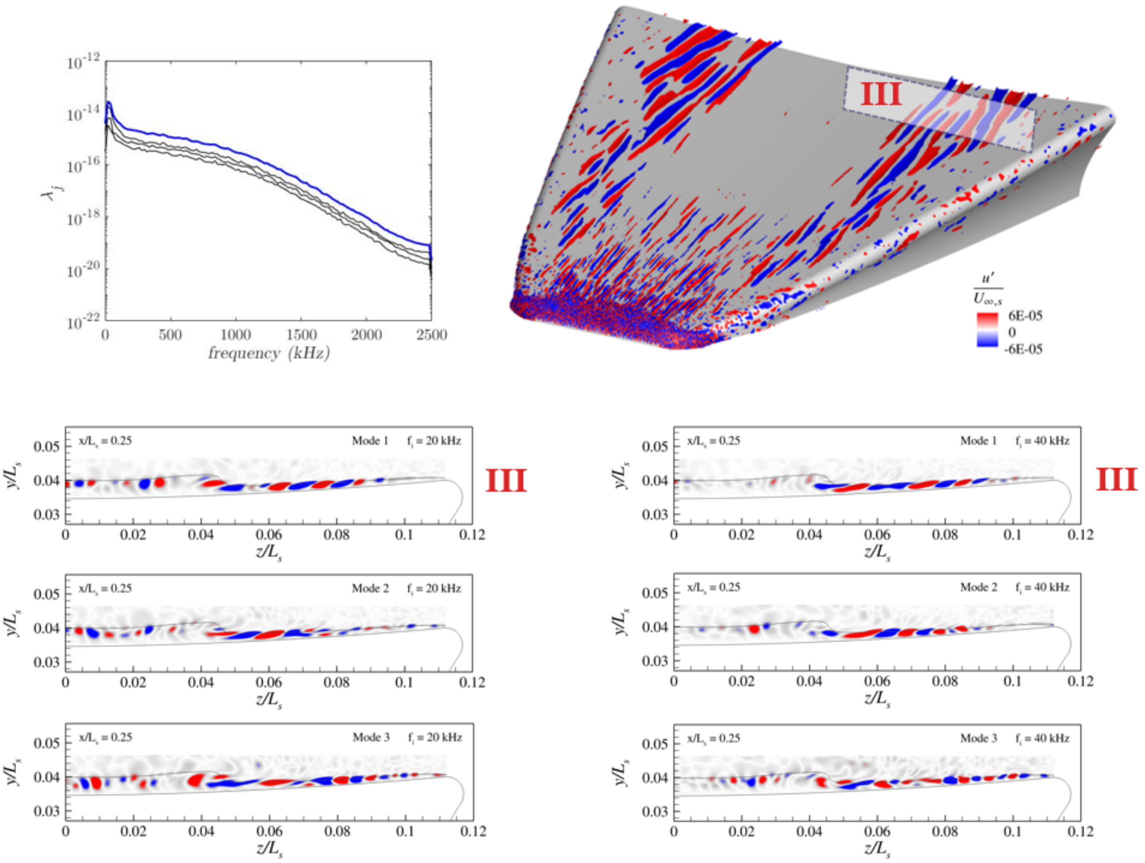

Figure 13: Leading SPOD Modes of the subscale configuration at $x/L_s = 0.25$

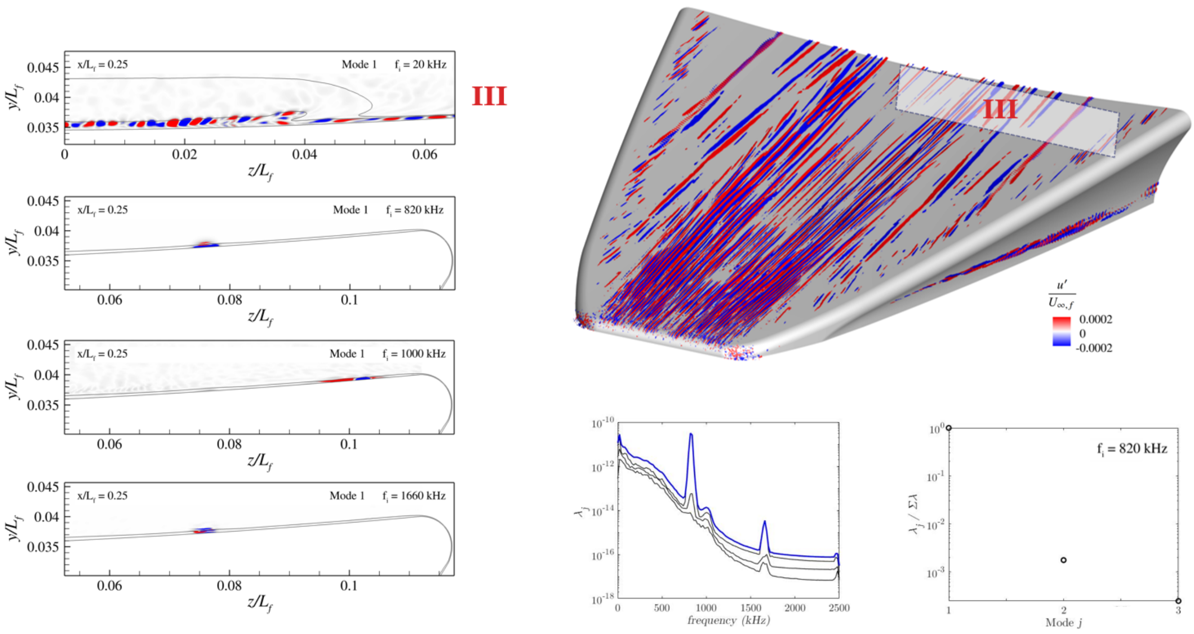

Figure 14: Leading SPOD Modes of the flight configuration at $x/L_f = 0.25$

6.3 Transition at Flight Condition

As mentioned previously, the grid spacing near the end of the domain is larger than what is required to properly resolve the turbulent length scales. However, we are still able to resolve relevant instabilities within the boundary layer with the current resolution. Most noticeable are instabilities found within the strong shears layers of the vortical structures near the centerline, and distinct structures associated with multiple types of instabilities between the centerline and swept leading edge. This is visualized in Fig. 15 with a single isosurface plotted of Q-criterion ($Q = 10,000$) and colored by normalized streamwise velocity on the left. While an instantaneous surface pressure perturbation distribution relative to the time-averaged wall value is plotted with a grey scale on the right. The largest magnitude in pressure perturbations is located near the centerline at which downstream of $x/L_f \approx 0.75$ the centerline vortical structures become unsteady. The sampling duration is $T_f u_\tau/\delta_i > 18$ and sampling frequency is $T_s u_\tau/\delta_i < 0.025$; where T_f is the time accumulated to collect statistics, T_s is the time between snapshots, δ_i is the maximum boundary layer thickness, and u_τ is the local friction velocity at δ_i. A higher sampling frequency would be required to properly collect turbulent flow statistics. In this work, the sampling is adequate for extracting meaningful SPOD modes and datasets already require large amounts of storage and resources to post-process.

In the following sections, we extract SPOD modes from flow state perturbations relative to the time-averaged values allowing us to identify the relevant modes contributing to transition. Therefore, current downstream analysis is meant to act as a starting point to shed light on the types of instabilities contributing to transition at a flight condition near regions of highest disturbance amplification using the introduced numerical methodology.

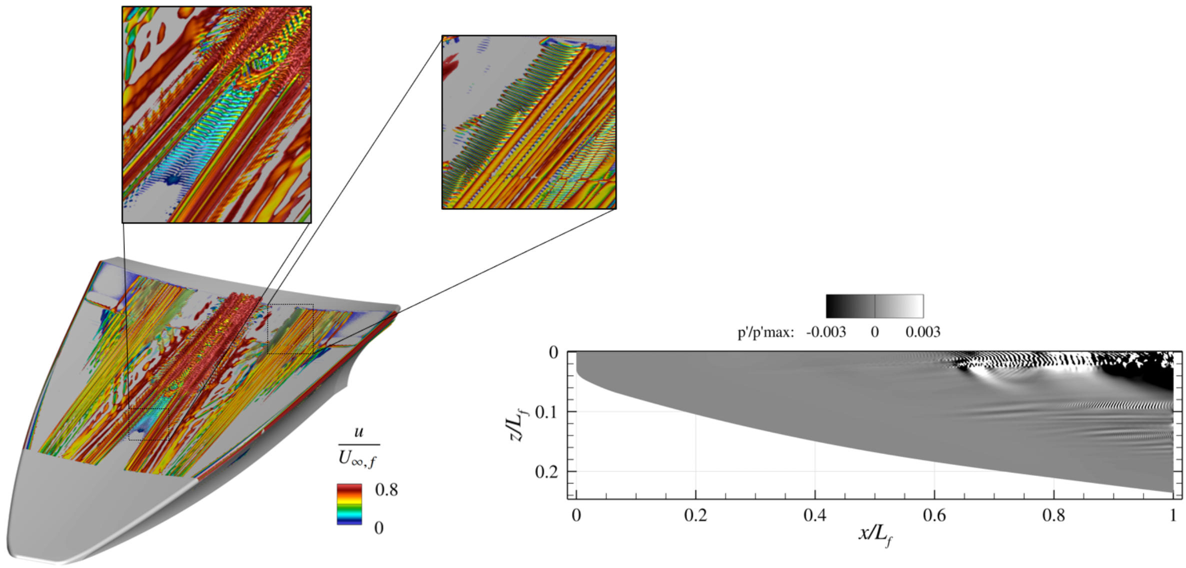

Figure 15: Q-criterion isosurface colored by normalized streamwise velocity (left). Instantaneous wall pressure fluctuations are normalized by the maximum pressure fluctuation on the wall (right).

6.3.1 Mixed Mode Region

The so called "mixed-mode" region in this work refers to the region away from the large-scale vortical structures and swept leading edge. The region contains distinct structures corresponding to both highly amplified acoustic waves and crossflow instabilities. Five separate slice datasets were collected at x/L_f=0.77, 0.88, 0.93 and z/L_f=0.089, 0.135 were then truncated within $x/L_f \ \epsilon \ [0.77, 0.93]$ and $z/L_f \ \epsilon \ [0.08, 0.16]$ to isolate the region. If the centerline region is included for the analysis, peaks in the modal energy spectrum are significantly attenuated since breakdown occurs near the centerline downstream as will be shown in the following section. SPOD is then performed on all slices to capture how the dominant modes are correlated in space and time. Fig. 16 shows peaks in the modal energy spectrum in the low frequency range between 11 kHz to 46 kHz and high frequency range between 295 kHz to 310 kHz.

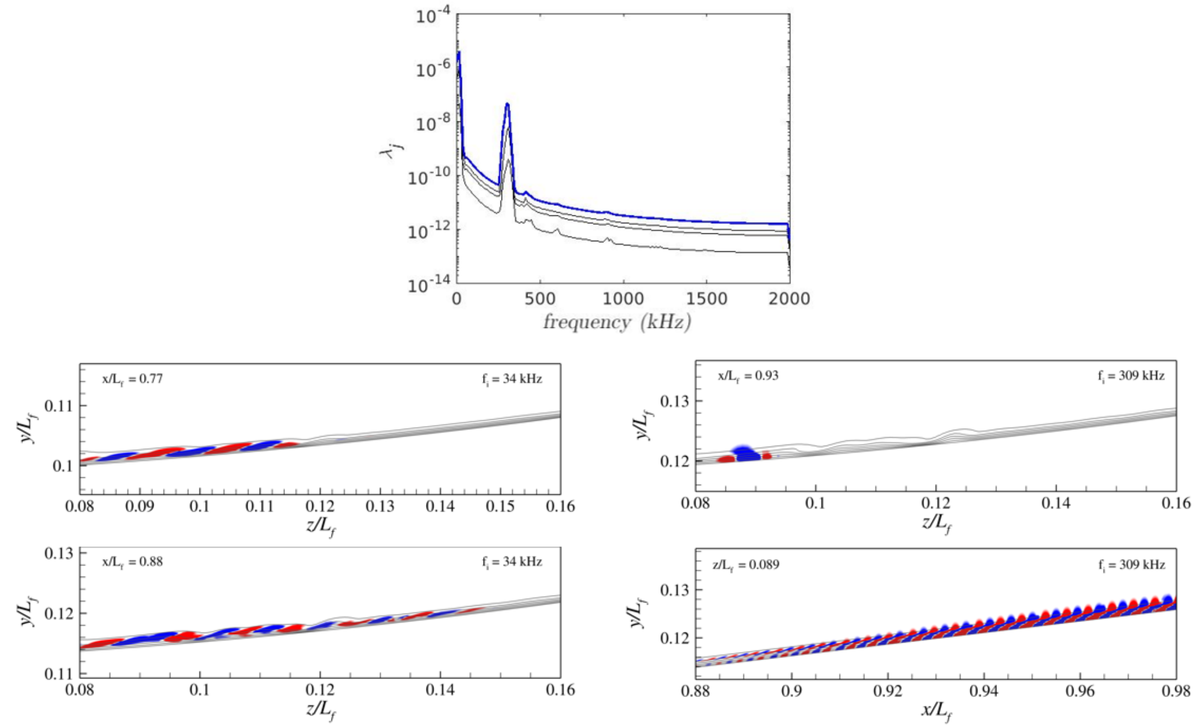

Figure 16: Dominant SPOD modes of the flight configuration between $x/L_f \ \epsilon \ [0.77, 0.93]$ and $z/L_f \ \epsilon \ [0.08, 0.16]$. Contour lines correspond to the time-averaged streamwise velocity of the dataset.

The value of 11 kHz in the modal energy spectrum is a peak at the sampling duration cutoff. It is likely a numerical artifact since the mode shapes contain insignificant signatures where transition occurs. It is possible that this could be due to sampling or from utilizing a sustained, stochastic forcing function since this behavior is primarily observed for SPOD results which include regions where slowly varying flow structures are present. This was checked previously by sampling for longer duration to ensure the low frequency modes converged to the same modal energy peaks. For this section, the lower frequency peak value ranges primarily between 23 kHz and 46 kHz which is a typical range for travelling crossflow frequencies on this geometry. This is because travelling crossflow has a strong presence across the entire vehicle surface and so appears to have a larger modal energy peak. Fig. 16 shows a travelling crossflow SPOD mode of 34 kHz on the left and is similar to DMD mode shapes of travelling crossflow [17, 1]. This mode is primarily located in the region of highest local disturbance energy of the mixed-mode region even though the surface pressure perturbations have lower perturbations relative to a highly localized region at $z/L_f = 0.089$. The highly localized exponential growth in surface pressure perturbations corresponds to the high frequency SPOD mode of 309 kHz. This mode has similar features of second-mode and scales as $f\frac{\delta}{u_e} \approx 0.35$ (at $x/L_f = 0.93$ and $z/L_f =$

0.089) using the streamwise wavelength of $\lambda_\zeta = 4.38$ mm. Using the mode shapes to calculate the spanwise wavelength gives $\lambda_\xi = 6.72$ mm where the wave angle is 32.7°. The mode shapes suggests there is a modal interaction since the second-mode disturbances in the region are oblique and coexist with a crossflow presence. This suggests second-mode disturbances have significant amplification for BoLT-2 at higher Reynolds numbers. When at lower Reynolds number conditions, the flow state tends to favor the amplification of crossflow instabilities but requires a large initial disturbance amplitude to initiate breakdown [1].

6.3.2 Vortical Mode Region

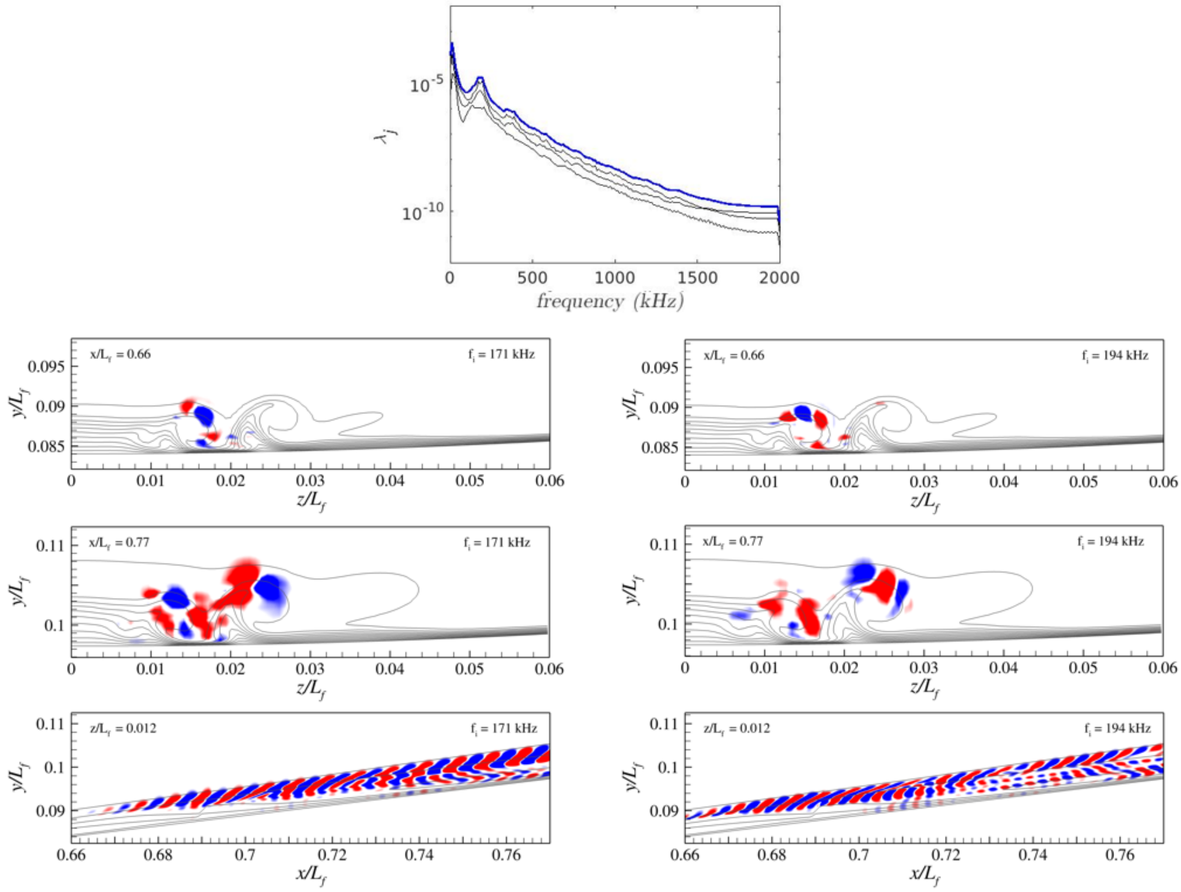

Figure 17: Dominant SPOD modes of the flight configuration between $x/L_f \in [0.55, 0.77]$ and $z/L_f \in [0, 0.06]$. Contour lines correspond to the time-averaged streamwise velocity of the dataset.

The vortical mode region in this work is referred to as the region containing the centerline roll-up illustrated by the bottom, left plot of Fig.7. The vortical structures have been shown to support vortical instabilities in the past for the subscale BoLT geometry [17] and is therefore named for consistency. Similar to the previous section, five separate slice datasets were collected but now at x/L_f=0.55, 0.66, 0.77 and z/L_f=0.012, 0.0235 then truncated within $x/L_f \in [0.55, 0.77]$ and $z/L_f \in [0, 0.06]$. For brevity we are only plotting modes which contain the highest energy gain and are located in the region where the largest flow perturbations are present. This is the most unstable region within the boundary layer where breakdown is initiated with the current numerical forcing approach. The centerline region is primarily dominated by high frequency vortical modes between 170 kHz and 200 kHz originating on the top portion of the primary vortex structure closest to the centerline. Significant exponential disturbance growth is observed at which the vortical structures become unsteady and eventually breakdown further downstream. Upstream of breakdown, a 171 kHz mode is located on the right side portion of the vortical structure closest to the centerline. Whereas, a 194 kHz is on the top portion of the same vortical structure. The SPOD mode shapes are similar to the DMD mode shapes of a crossflow vortex structure for the subscale BoLT-2 geometry [1]. Both of which are similar to the excitation of secondary instability mechanisms of stationary crossflow vortices of a swept wing [29].

7 Conclusion

Boundary layer instabilities associated with distinct transition mechanisms of the BoLT-2 flowfield were identified using SPOD and ranked by their modal energy gain. This was intended to quantify how the disturbances of the receptivity process may contribute to the later stages of the transition process at flight conditions where the boundary layer is likely to be in a transitional state. This was achieved by performing high-fidelity computations of the Navier-Stokes equations using a low-dissipation numerical method within US3D. Furthermore, we introduced disturbances using a stochastic forcing function at the freestream to allow for a boundary layer response revealing modal and non-modal growth mechanisms that exist within the BoLT-2 flowfield. The most notable SPOD modes near the nosetip are associated with low frequency, non-modal growth mechanisms contained within the centerline rollup of the boundary layer for both the subscale and flight configurations. The perturbations were found to be much larger for the full-scale configuration at flight conditions, suggesting the non-modal growth mechanisms could potentially contribute to early transition at high Reynolds numbers.

Modal growth mechanisms were identified slightly further downstream of the nosetip. The subscale configuration contained leading SPOD modes associated with travelling crossflow, while the flight configuration had dominant SPOD modes corresponding to Mack's second mode disturbances. This suggests second-mode disturbances are increasingly susceptible to amplification on the BoLT-2 geometry with higher Reynolds numbers at hypersonic conditions. Additionally, we were able to identify leading modes contributing to transition downstream within the centerline vortical structures and mixed-mode region. It was found that high-frequency disturbances in the range between 170 kHz and 200 kHz initiate breakdown near the centerline and are primarily localized near shear layers of streamwise vortex stuctures. While breakdown was not observed in the mixed-mode region using the current methodology, we were still able to identify crossflow and second-mode structures.

The current work provides insight for instabilities that may be present in flight. However, future work regarding disturbances sources should be investigated for improved prediction of transition in flight. Freestream turbulence and particulate induced transition have both been shown to be potential sources of transition in flight and would represent a more realistic disturbance environment. Although, in order to properly model passing disturbances through the shock the orthogonality at the shock should also be addressed. The wall-normal grid connected cell alignment at the shock location would require a three-dimensional shock-fitting approach or a shock-kinematic boundary condition approach to ensure complete orthogonality. Shock fitting is an active area of code development and the extension to the unstructured, three dimensional numerical solver has not progressed to the application to the current work of this paper. Future work related to passing disturbances through three-dimensional shocks should account for this and the contribution of the error to the solution quantified. Furthermore, we are assuming a smooth and isothermal wall boundary condition. Both roughness [2] and variable wall temperature [30] can have a significant impact on the boundary layer state and future work could extend the parameter space for improved transition prediction. Nevertheless, the current approach is able to investigate the stability of unsteady, three-dimensional flow structures and identify potentially relevant instability mechanisms contributing to transition in flight.

Acknowledgments

This work was supported by the Hypersonic Vehicle Simulation Institute (HVSI), the Collaborative Center for Aerospace Sciences (CCAS) and the Air Force Office of Scientific Research (AFOSR) under award number FA9550-21-1-0106. The views and conclusions contained herein are those of the authors and should not be interpreted as necessarily representing the official policies or endorsements, either expressed or implied, of the AFOSR or the U.S Government.

References

[1] Johnston Z. M., Hemati M. S., and Candler, G. V. "Modal Analysis of Instabilities in the BoLT-2 Flowfield," AIAA SCITECH 2022-0348

[2] Thome, J. S., Reinert, J. D., and Candler, G. V. "Effect of steady forcing on BoLT flowfield for flight Reynolds Numbers," AIAA 2020-1042

[3] Thome J. S., Private Communication, 2020

[4] Melander, L. J., Dwivedi, A., and Candler,G. V. "Nose Bluntness Effects on the Amplification of External Disturbances in Hypersonic Flows," AIAA 2022-0948.

[5] Wheaton B. M., Berridge D. C., Wolf T. D., Stevens R. T., and McGrath B. E. "Boundary Layer Transition (BoLT) Flight Experiment Overview," AIAA AVIATION 2018-2892

[6] Mullen, D. and Reed, H. L. "Analysis of the BoLT-2 Holden Mission Flight and Wind Tunnel Geometries," AIAA SCITECH 2021-0852

[7] Candler G. V., Barhhardt M. D., Drayna T. W., Nompelis I., Peterson D. M., and Subbareddy P. K. "Unstructured grid approaches for accurate aeroheating simulations," AIAA Paper, Vol. 3959, 2007

[8] Subbareddy P. K., Bartkowicz M. D., and Candler G. V., "Direct numerical simulation of high-speed transition due to an isolated roughness element," J. Fluid Mech., Vol. 748, pp. 848-878, 2014

[9] Subbareddy, P. K. and Candler, G. V. "A fully discrete, kinetic energy consistent finite-volume scheme for compressible flows," *Journal of Computational Physics*, Vol. 228, No. 5, pp. 1347-1364, 2009

[10] MacCormack, R. W. and Candler, G. V. "The solution of the Navier-Stokes equations using Gauss-Seidel line relaxation," Computers & Fluids, Vol. 17, No. 1, pp 135-150, 1989

[11] Nompelis, I., "Computational study of hypersonic double-cone experiments for code validation," Ph. D. thesis, University of Minnesota, 2004

[12] Knutson, A. L., Sidharth G. S., and Candler, G. V. "Instabilities in Mach 6 Flow over a cone with a Swept Fin," AIAA 2018-3071

[13] Wright, M. J., Candler, G. V., and Bose, D. "Data-parallel line relaxation method for the Navier-Stokes equations," *AIAA Journal*, Vol. 36, No. 9, pp. 1603-1609, 1998

[14] Knutson, A. L. "Numerical Simulation of Instabilities in Three-Dimensional Hypervelocity Boundary Layers," Ph. D. thesis, University of Minnesota, 2020

[15] Johnston Z. M. and Candler, G. V. "Hypersonic simulations of the BoLT-2 subscale geometry," AIAA SCITECH 2021-0366

[16] Thome J. S., Knutson A. L., and Candler, G. V. "Boundary layer instabilities on BoLT subscale geometry," AIAA SCITECH 2019-0092

[17] Knutson, A. L., Thome T. S., and Candler, G. V. "Numerical Simulation of Instabilities in the Boundary-Layer Transition Experiment Flowfield," *Journal of Spacecraft and Rockets*, Vol. 58, pp. 90-99, 2020

[18] Cook, D. A. and Nichols, J. W. "Free-stream receptivity of a hypersonic blunt cone using input–output analysis and a shock-kinematic boundary condition," *Theoretical and Computational Fluid Dynamics*, Vol. 36, pp. 155-180, 2022

[19] Chu. B. T. "On the energy transfer to small disturbances in fluid flow (Part I)," *Acta Mechanica*, Vol. 1, No. 3, pp. 215-234, 1965

[20] Lumley, J. L. "Stochastic tools in turbulence," Courier Corporation, 2007

[21] Towne, A., Schmidt, O. T., and Colonius, T. "Spectral proper orthogonal decomposition and its relationship to dynamic mode decomposition and resolvent analysis," *J. Fluid Mech.*, Vol. 847, pp. 821-867, 2018

[22] Schmidt, O. T. and Colonius, T. "Guide to Spectral Proper Orthogonal Decomposition," *AIAA Journal*, Vol. 58, No. 3, pp. 1023-1033, 2020

[23] Pirozzoli, S. and Orlandi, P. "Natural grid stretching for DNS of wall-bounded flows," *Journal of Computational Physics*, Vol. 439, 2021

[24] Bitter N. and Shepherd, J. "Transient Growth in Hypersonic Boundary Layers," *7th AIAA Theoretical Fluid Mechanics Conference*, pp. 2497, 2014.

[25] Landahl, M. "Dynamics of boundary layer turbulence and the mechanism of drag reduction," *Physics of Fluids*, Vol. 20, No. 10, pp. S55-S63, 1977

[26] Dwivedi, A., Sidharth, G. S., Nichols, J. W., Candler, G. V., and Jovanovic, M. R. "Reattachment streaks in hypersonic compression ramp flow: an input-output analysis," *J. Fluid Mech.*, Vol. 880, pp. 113-135, 2019

[27] Dinzl, D. J. and Candler, G. V. "Direct simulation of hypersonic crossflow instability on an elliptic cone," *AIAA Journal*, Vol. 55, No. 6, pp. 1769-1782, 2017

[28] Stetson, K. F. "Hypersonic Boundary-Layer Transition," *Advances in Hypersonics*, Springer, New York, pp. 324-417, 1992

[29] Chen, J., Dong, S., Chen, X., Yuan, X., and Xu, G. "Stationary cross-flow breakdown in a high-speed swept-wing boundary layer," *Physics of Fluids*, Vol. 33, 024108, 2021

[30] Reinert, J. D. "Conjugate Heat Transfer Simulations for Hypersonic Vehicles," Ph. D. thesis, University of Minnesota, 2020